Refreezing of Partially Melted Hydrometeors: Polarimetric Radar Observations and Microphysical Model Simulations

DANA M. TOBIN,[a] MATTHEW R. KUMJIAN,[a] MARIKO OUE,[b] AND PAVLOS KOLLIAS[b,c]

[a] Department of Meteorology and Atmospheric Science, The Pennsylvania State University, University Park, Pennsylvania
[b] School of Marine and Atmospheric Sciences, Stony Brook University, State University of New York, Stony Brook, New York
[c] Brookhaven National Laboratory, Upton, New York

(Manuscript received 11 August 2022, in final form 11 October 2022)

ABSTRACT: The discovery of a polarimetric radar signature indicative of hydrometeor refreezing has shown promise in its utility to identify periods of ice pellet production. Uniquely characterized well below the melting layer by locally enhanced values of differential reflectivity (Z_{DR}) within a layer of decreasing radar reflectivity factor at horizontal polarization (Z_H), the signature has been documented in cases where hydrometeors were completely melted prior to refreezing. However, polarimetric radar features associated with the refreezing of *partially melted* hydrometeors have not been examined as rigorously in either an observational or microphysical modeling framework. Here, polarimetric radar data—including vertically pointing Doppler spectral data from the Ka-band Scanning Polarimetric Radar (KASPR)—are analyzed for an ice pellets and rain mixture event where the ice pellets formed via the refreezing of partially melted hydrometeors. Observations show that no such distinct localized Z_{DR} enhancement is present, and that values instead decrease directly beneath enhanced values associated with melting. A simplified, explicit bin microphysical model is then developed to simulate the refreezing of partially melted hydrometeors, and coupled to a polarimetric radar forward operator to examine the impacts of such refreezing on simulated radar variables. Simulated vertical profiles of polarimetric radar variables and Doppler spectra have similar features to observations, and confirm that a Z_{DR} enhancement is not produced. This suggests the possibility of two distinct polarimetric features of hydrometeor refreezing: ones associated with refreezing of completely melted hydrometeors, and those associated with refreezing of partially melted hydrometeors.

SIGNIFICANCE STATEMENT: There exist two pathways for the formation of ice pellets: refreezing of fully melted hydrometeors, and refreezing of partially melted hydrometeors. A polarimetric radar signature indicative of fully melted hydrometeor refreezing has been extensively documented in the past, yet no study has documented the refreezing of partially melted hydrometeors. Here, observations and idealized modeling simulations are presented to show different polarimetric radar features associated with partially melted hydrometeor refreezing. The distinction in polarimetric features may be beneficial to identifying layers of supercooled liquid drops within transitional winter storms.

KEYWORDS: Winter/cool season; Ice particles; Mixed precipitation; Radars/Radar observations; Idealized models

1. Introduction

Winter precipitation can pose varying surface hazards depending on whether the precipitation is frozen (i.e., snow, ice pellets) or freezing (i.e., freezing rain, freezing drizzle), with freezing precipitation being significantly more destructive (e.g., Zerr 1997; Rauber et al. 1994, 2001). Freezing precipitation can produce ice accumulations on tree limbs and infrastructure including utility lines, causing them to sag and snap (e.g., Bennett 1959; Bendel and Paton 1981). It can also create slick, hazardous conditions for motorists, increasing their risk of motor vehicle crashes and casualties (Tobin et al. 2021). Ice storms—winter storms that produce ≥0.25 in. (≥6.4 mm) of ice accumulation on exposed surfaces—are among the most destructive winter storms, with annual insured property losses totaling over $478.8 million[1] in the United States, accounting for ~60% of all winter storm losses (Changnon 2003).

Ice pellets reach the surface as frozen precipitation, yet they originate as snowflakes that fully or partially melt within an elevated layer of >0°C wet-bulb temperature (T_w), and freeze within a near-surface $T_w < 0$°C layer (e.g., Brooks 1920; Hanesiak and Stewart 1995; Zerr 1997). Partially melted hydrometeors immediately begin to refreeze within the $T_w < 0$°C near-surface layer; however, in the case of complete melting, liquid hydrometeors remain supercooled until ice is later nucleated within them. Thus, there exist two pathways for the formation of ice pellets at the surface. Although this distinction has little consequence at the surface if hydrometeors are completely refrozen, it has profound impacts aloft. Aviation is particularly susceptible to the presence of supercooled liquid drops aloft, as many aircraft are not certified to fly in such conditions. In-flight icing is a significant hazard, as airframe ice accumulations can adversely affect aerodynamics and lead to loss of control.

Supplemental information related to this paper is available at the Journals Online website: https://doi.org/10.1175/JAS-D-22-0174.s1.

Corresponding author: Dana M. Tobin, dana.tobin@noaa.gov

[1] In year 2021 dollars, based on data from 1949 to 2000 (Changnon 2003).

DOI: 10.1175/JAS-D-22-0174.1

Approximately 10 in-flight icing incidents occur annually (Green 2015); though these incidents represent only a small portion of all aviation accidents, the ultimate goal of the Federal Aviation Administration (FAA) is to have zero accidents (FAA 1995). Identifying the presence of supercooled liquid drops aloft thus remains a priority of the FAA (DiVito and Riley 2017), and the use of polarimetric radar is a leading contender for addressing this need (e.g., Plummer et al. 2010; Serke et al. 2013; Bernabó et al. 2016; Reeves and Waters 2019).

After the polarimetric upgrades to the National Weather Service's network of Weather Surveillance Radar-1988 Doppler (WSR-88D) radars, an unexpected and unique signature indicative of hydrometeor refreezing was observed during numerous ice pellet events (e.g., Kumjian et al. 2013, 2020; Kumjian and Schenkman 2014; Ryzhkov et al. 2016; Van Den Broeke et al. 2016; Tobin and Kumjian 2017, 2021). Kumjian et al. (2013) define the refreezing layer (RFL) as the layer of decreasing radar reflectivity factor at horizontal polarization (Z_H) toward the ground, attributed to the change in hydrometeor relative permittivity from liquid to ice as freezing progresses within the $T_w < 0°C$ near-surface layer. A local enhancement of differential reflectivity (Z_{DR}) was observed in the RFL, counter to the expectation that both variables would decrease owing to reduced Z_H values (Kumjian et al. 2013). Reductions in the copolar correlation coefficient (ρ_{hv}) were also observed due to diversity in particle type, shape, and canting angle with freezing (e.g., Kumjian et al. 2012, 2013). With a fully polarimetric research radar, Kumjian et al. (2020) documented locally enhanced linear depolarization ratio (LDR) values attributed to several possibilities: particle deformations (e.g., Gibson and Stewart 2007; Nagumo et al. 2019), asymmetric unfrozen regions within freezing particles, or anisotropic ice crystals. Originally, Kumjian et al. (2013) proposed two hypotheses for the signature: preferential refreezing of the smallest drops, and the presence of anisotropic ice crystals. While both fell short of fully explaining the polarimetric observations, the former was the favored hypothesis until Tobin and Kumjian (2021) concluded that preferential refreezing is insufficient to produce meaningful Z_{DR} enhancements. Instead, they proposed that the signature is dependent upon the geometry of the inner unfrozen region of freezing hydrometeors. Namely, asymmetric freezing rates around a stably oriented, ventilated particle can produce an overly oblate unfrozen region due to the formation of a thicker ice shell on the particle's bottom (upwind side). Scattering calculations performed therein based on that hypothesis successfully replicated the salient features of the polarimetric refreezing signature. Ultimately, the role of anisotropic ice crystals in the signature remains uncertain (Kumjian et al. 2013, 2020; Tobin and Kumjian 2021).

Whereas there are two distinct pathways for ice pellet formation—the refreezing of partially melted hydrometeors at $T_w < 0°C$ and the refreezing of fully melted hydrometeors at some lower T_w after nucleating ice—the polarimetric refreezing signature described above has only been documented and analyzed in the case of *fully melted* hydrometeor refreezing. In all reported cases, high ρ_{hv} values between the melting and refreezing layers suggest that hydrometeors had melted sufficiently to collapse into raindrop shapes, if not melted completely. Further, the top of the RFL was located at $T_w \leq -5°C$, several hundred meters beneath the $T_w = 0°C$ level at which partially melted hydrometeors would initiate refreezing. It remains unknown whether the signature is present during *all* cases of fully melted hydrometeor refreezing, or whether it represents only a subset of such cases. Regardless, there exists a gap in knowledge regarding the polarimetric features associated with the refreezing of *partially melted* hydrometeors. Here, we begin efforts to fill that void. First, we present polarimetric radar observations from a case where ice pellets formed after incomplete melting aloft. Second, we use a simplified one-dimensional microphysical model coupled to a polarimetric radar forward operator to explore the impacts of refreezing after partial melting on the radar signals. We conclude by comparing and contrasting the two refreezing pathways and their associated polarimetric radar features, and discuss the implications of any differences between the two.

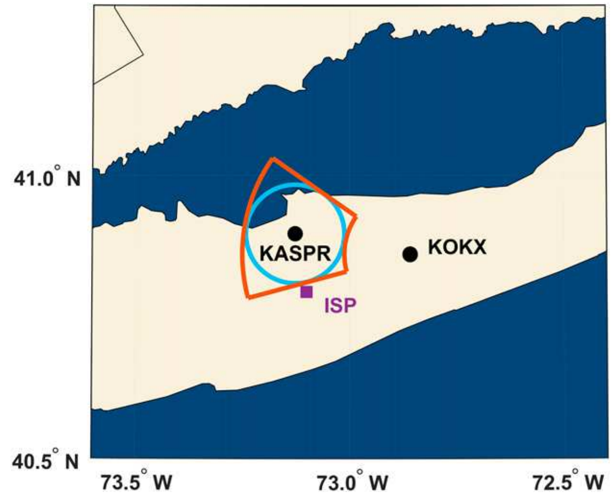

FIG. 1. Locations of the observation sites of interest, including the KASPR and KOKX radars (black dots), and the ISP ASOS site (purple square). Orange lines denote the limits within which range–azimuth-defined quasi-vertical profiles (raQVPs) are computed. The blue circle denotes the approximate range within which KASPR QVPs at 15° elevation angle are below 2500 m above radar level (ARL) in height.

2. Event and data overview

A transitional winter precipitation event featuring a long duration of concurrent ice pellets and rain occurred over central Long Island on 17 December 2019. This storm was observed by the Stony Brook University and Brookhaven National Laboratory Radar Observatory Ka-band Scanning Polarimetric Radar (KASPR; Kollias et al. 2020; Kumjian et al. 2020) in Stony Brook, New York, and the nearby S-band WSR-88D radar in Upton, New York (KOKX), <25 km away. KASPR and KOKX are situated near the Automated Surface Observing System (ASOS) at Long Island MacArthur Airport (ISP; Fig. 1). ISP reports were augmented by a human observer throughout the event, which provides an accurate account of all precipitation types that is crucial for this study. ASOS sites without human observers present to manually augment reports are unable to report ice pellets or precipitation-type mixtures (NOAA 1998).

KASPR has high sensitivity and provides high-resolution data ideal for winter-precipitation analyses (e.g., Oue et al. 2017, 2021; Kumjian et al. 2020). On 17 December, it operated with a scanning strategy taking ~7.5 min to complete, including a plan position indicator (PPI) surveillance scan at 15° elevation angle, and observations collected in a vertically pointing (VPT) mode. During VPT mode, Doppler spectra were collected nearly every second for ~2.5 min. Quasi-vertical profiles (QVPs; e.g., Kumjian et al. 2013; Ryzhkov et al. 2016) were constructed as the azimuthal average of the 15° elevation angle PPI scans at each range gate, with range converted to height above the radar. These profiles provide vertical representations of the polarimetric radar variables, and are useful for displaying observations in time–height format to reveal the evolution of the average vertical precipitation structure.

With the S-band KOKX radar in close proximity, it is useful to compare data between the two radars. KASPR operates at a higher frequency (35 GHz) than the 2.7-GHz KOKX radar, making KASPR more prone to attenuation in heavy precipitation and resonance scattering effects for large, wetted particles, such as melting snowflakes near the top of the melting layer (e.g., Kollias and Albrecht 2005; Kollias et al. 2007). However, KASPR collects finer-resolution data (e.g., 0.32° beamwidth versus 0.925°), and performs VPT scans, which KOKX does not. Last, KASPR alternates transmission of two orthogonally polarized signals while receiving signals from both polarizations, allowing measurements of LDR in addition to the variables available from KOKX (e.g., Z_H, Z_{DR}, ρ_{hv}). To mitigate the effects of spatial displacement while still providing the visualization benefits of QVPs, range- and azimuth-defined QVPs (raQVPs; e.g., Tobin and Kumjian 2017) are computed with KOKX radar data within the sampling volume represented in Fig. 1. This volume is chosen to correspond with the approximate range of the KASPR QVPs at 2500 m above radar level (ARL; all heights are ARL hereafter, relative to KASPR's altitude), assuming standard beam refraction (e.g., Doviak and Zrnić 1993).

For the mixture event, particular emphasis is placed on the insights afforded by Doppler spectral analysis in VPT mode, as it provides information on hydrometeor phase, and can give insights into precipitation type formation. The Doppler spectrum is defined as the reflectivity-weighted distribution of the radial velocities of scatterers within a sampling volume (e.g., Doviak and Zrnić 1993). The units of spectral reflectivity are $\mathrm{mm^6\ m^{-3}\ (m\ s^{-1})^{-1}}$. There is no formally accepted unit in dB scaling (Li and Moisseev 2020), so units of dBZ are used for consistency with Z_H. Similarly, spectral LDR are shown with units of dB. Doppler spectral data are presented as height–velocity depictions, or spectrographs, of equivalent radar reflectivity Z_e and LDR in Doppler velocity increments of ~0.16 m s^{-1}, where negative radial velocities denote scatterers approaching the radar (i.e., falling). Reflectivities Z_H and Z_e are equivalent measures of the signal returned to the radar, but we maintain the distinction as Z_H and Z_e denoting power received at side and vertical incidence, respectively. A −85-dB co- and cross-polar power threshold is applied to the spectral data to remove some noise (e.g., Kumjian et al. 2020).

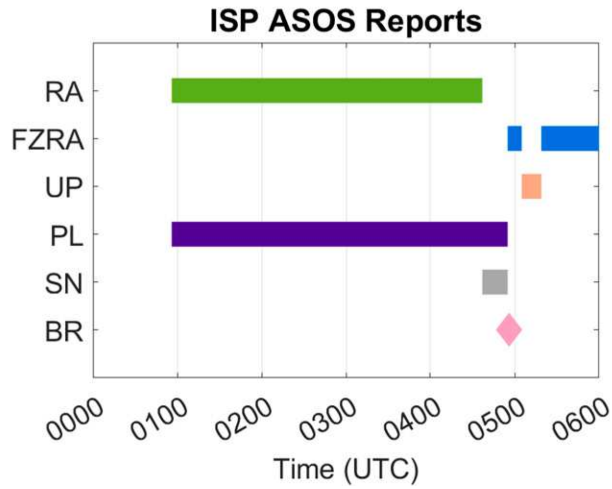

FIG. 2. Human-augmented ASOS reports from ISP between 0000 and 0600 UTC 17 Dec 2019. The time intervals of each precipitation type are denoted by colored lines separated by precipitation type report on the ordinate axis as rain (RA; green lines), freezing rain (FZRA; blue lines), unknown precipitation (UP; salmon lines), ice pellets (PL; purple lines), and snow (SN; gray lines). A report of mist (BR) is denoted by a pink diamond.

3. Observations

On 17 December 2019, both rain and ice pellets were reported beginning at the onset of precipitation at 0056 UTC until 0437 UTC, when it transitioned to wintry precipitation mixtures (Fig. 2). KOKX raQVPs (Fig. 3) and KASPR QVPs (Fig. 4) depict a melting layer near 2000 m ARL during the event, marked by enhancements in Z_H, Z_{DR}, and LDR, and a ρ_{hv} reduction. Peak S-band Z_H values in the melting layer are >35 dBZ, whereas KASPR depicts the melting layer with a sharp increase in Z_H to ~25 dBZ with no significant reduction below, owing to resonance scattering effects in large, melting aggregates. Z_H values above the melting layer are lower for KASPR than for the KOKX radar owing to resonance scattering and attenuation through the melting layer at Ka band. A prominent Z_{DR} enhancement and ρ_{hv} reduction accompany the melting layer in both radar profiles, and an LDR enhancement is present in the KASPR QVPs. Resonance scattering effects are also to blame for the lower KASPR ρ_{hv} values, whereas attenuation and Z_{DR} calibration differences between the two radars are to blame for the slightly higher Z_{DR} values throughout the profile. Refreezing is indicated by a reduction in all variables toward the ground below ~650 m. This is distinct from previously documented cases of refreezing where a prominent Z_{DR}

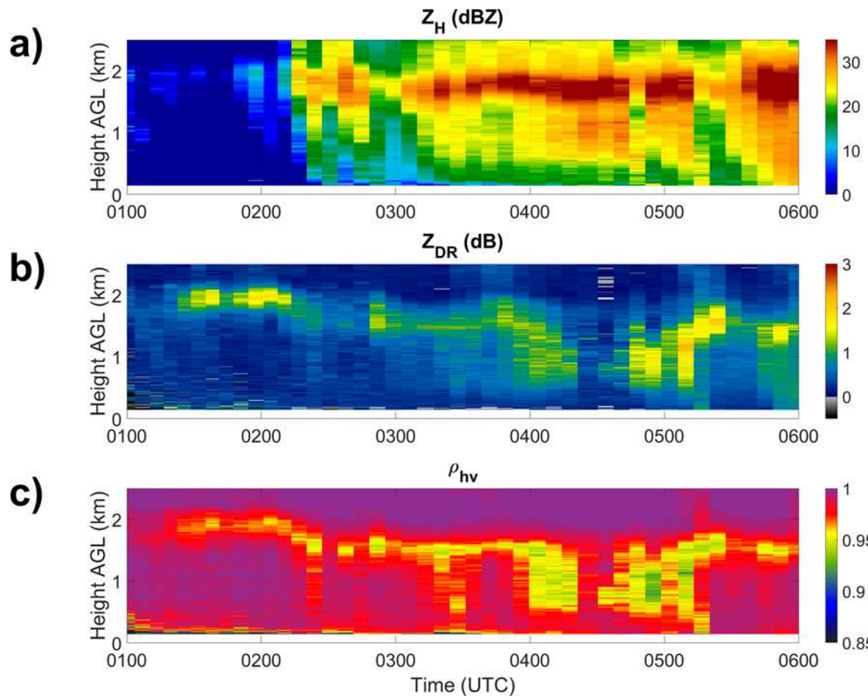

FIG. 3. KOKX raQVPs of (a) Z_H, (b) Z_{DR}, and (c) ρ_{hv} from 0100 to 0600 UTC 17 Dec 2019, constructed from the data in the orange-outlined volumetric sector of Fig. 1. Heights are relative to KASPR's altitude.

enhancement is present in QVPs[2] (e.g., Kumjian et al. 2013, 2020; Ryzhkov et al. 2016; Van Den Broeke et al. 2016; Tobin and Kumjian 2017).

Unfortunately, this case does not have reliable thermodynamic information throughout the event. Hourly Rapid Refresh (RAP; Benjamin et al. 2016) model analysis T_w profiles closest to the KASPR radar location are shown in Fig. 5, along with T_w profiles from the 0000 and 1200 UTC soundings at KOKX.[3] A $T_w > 0°C$ layer with a depth > 50 m aloft is not indicated in the RAP profiles until 0400 and 0600 UTC, yet the 0500 UTC model analysis again produces a T_w profile entirely <0°C. Given the evident melting layer signatures in the radar observations between 0100 and 0600 (Figs. 3 and 4), the RAP model profiles are likely cold biased for much of the event. Such temperature biases near an observed melting layer are, unfortunately, common during winter precipitation (e.g., Griffin et al. 2014; Kumjian and Lombardo 2017; Tobin and Kumjian 2017). With such biases, it is difficult to discern the top and thus depth of the near-surface $T_w < 0°C$ layer, in addition to the depth and strength of the overlying $T_w > 0°C$ melting layer.

Animations of Doppler spectral Z_e and LDR (see online supplemental material for an example) are uniform in time and contain similar features among scans from approximately 0300 to 0420 UTC, a period with both ice pellets and rain reported at ISP. Freezing rain shortly after this long duration of ice pellets and rain provides a unique opportunity to compare the two precipitation-type periods. The comparison of the all-liquid spectral data to the ice-pellet-and-liquid mixture spectra can provide insights into the ice pellet "fingerprint" within the spectra as a means to distinguish the two precipitation types. Given that both precipitation-type periods occurred within hours of each other as part of the same synoptic-scale system, the microphysical differences aloft between the two periods should be minimal in terms of precipitation intensity and the types of hydrometeors falling into the melting layer. Indeed, Z_H values from KOKX above the melting layer during both periods are comparable (not shown). For the analysis, we begin with the freezing rain period (the chronologically later period) to compare against the ice-pellets-and-rain period (the chronologically earlier period) that is the focus of our study.

a. *Doppler spectra at 0555 UTC: Freezing rain period*

Thirty-second-averaged Doppler spectrographs of Z_e and LDR at 0555 UTC are shown in Fig. 6. No fall streaks were evident in the time–height VPT depictions (not shown), so short temporal averages over the homogeneous period are appropriate, and help to further reduce noise. As such, these 30-s averages smooth out some temporal variability within the spectra and bring out the dominant spectral features of interest. Melting is first indicated around 2000 m as an increase in Z_e and LDR, and then as a rapid increase in particle fall

[2] Periods of slightly enhanced Z_{DR} values after 0315 UTC in both radars are not related to a refreezing signature, as these enhancements are collocated with enhanced ZH.

[3] T_w was estimated following Stull (2011).

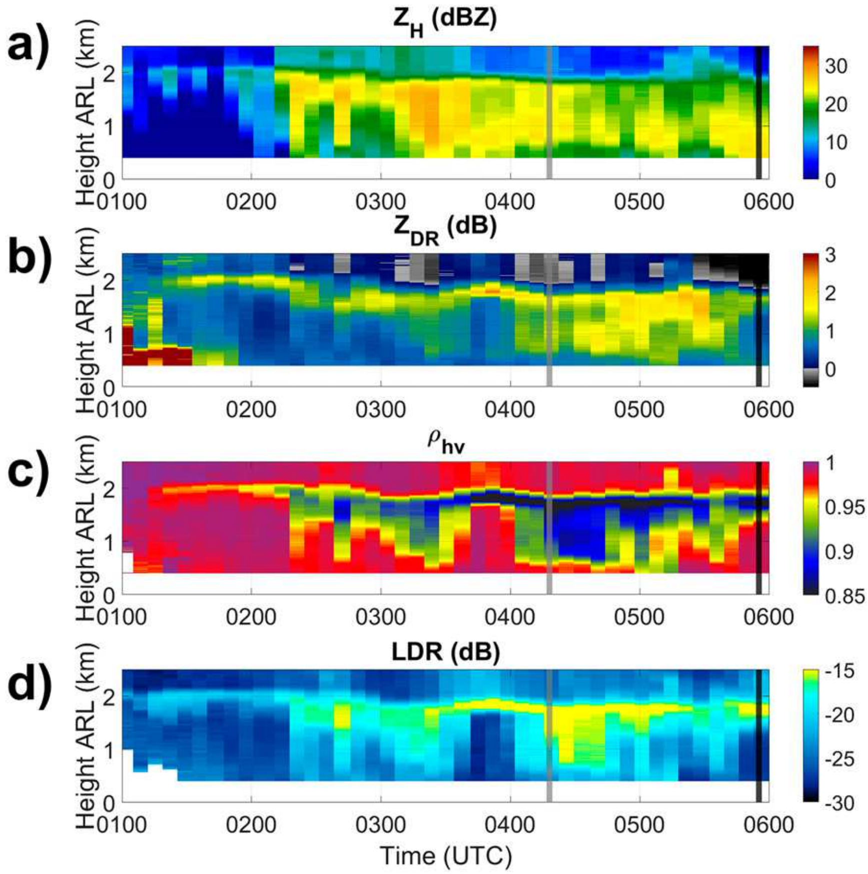

FIG. 4. KASPR QVPs of (a) Z_H, (b) Z_{DR}, (c) ρ_{hv}, and (d) LDR from 0100 to 0600 UTC 17 Dec 2019. Dark and light gray lines denote the time of the spectrographs in Figs. 6 and 11, respectively.

speeds at 1800 m. The increase in LDR with melting implies particle asymmetry with no preferred orientation in the horizontal plane, meaning that the initially low LDR values aloft are due to low particle effective density instead of particle symmetry. This is consistent with Jiang et al. (2019) and Dunnavan et al. (2019), who, respectively, showed that aggregates are perhaps best represented as prolate spheroids or triaxial ellipsoids instead of oblate spheroids, as is often assumed (e.g., Matrosov et al. 2005; Kennedy and Rutledge 2011; Hogan et al. 2012; Moisseev et al. 2015). At ~1250 m, LDR is reduced near the system's lower limit (approximately −30 dB) for all particles, indicating that snowflakes have fully collapsed into raindrops by this height. This is because raindrops appear spherical when viewed from below, so intrinsic LDR = $-\infty$ dB. Z_e remains nearly constant within each velocity bin beneath this height, so there is no evidence for refreezing, consistent with reports of freezing rain at this time. The fall speeds of these fully melted particles range from 2.8 to 8.9 m s^{-1} between 1250 and 750 m, which correspond to liquid particle diameters of 0.7 and 3.8 mm (e.g., Brandes et al. 2002), assuming a 1.14 kg m^{-3} mean air density at these elevations, based on 0600 UTC RAP data. Such particle sizes are typical for stratiform rain, and have been observed during freezing rain events (e.g., Rahman and Testik 2020). The uniformity of Z_e with height for these fully melted hydrometeors in this layer suggests the absence of any significant changes to the drop size distribution due to evaporation, coalescence, or breakup processes. Beneath 750 m, however, unfiltered Z_e values are present at slower fall speeds, suggesting either particle breakup and the generation of larger concentrations of smaller droplets, or Doppler spectra broadening owing to boundary layer turbulence.

Examination of subsequent VPT scans revealed that the LDR enhancement's depth decreases, whereas Z_e values above the melting layer remain consistent in time (not shown). This evolution indicates a strengthening $T_w > 0°C$ layer with more-rapid particle melting. The opposite is true for earlier scans closer to the transition from ice pellets and rain to freezing rain, where the LDR enhancements are even deeper. The depth of these LDR enhancements seems to have key implications in the formation of ice pellets via partially melted hydrometeors: partially melted snowflakes that have not collapsed into raindrops have large LDR values, and begin to refreeze in the $T_w < 0°C$ near-surface layer. With these insights, we now examine the earlier period characterized by ice pellets and rain.

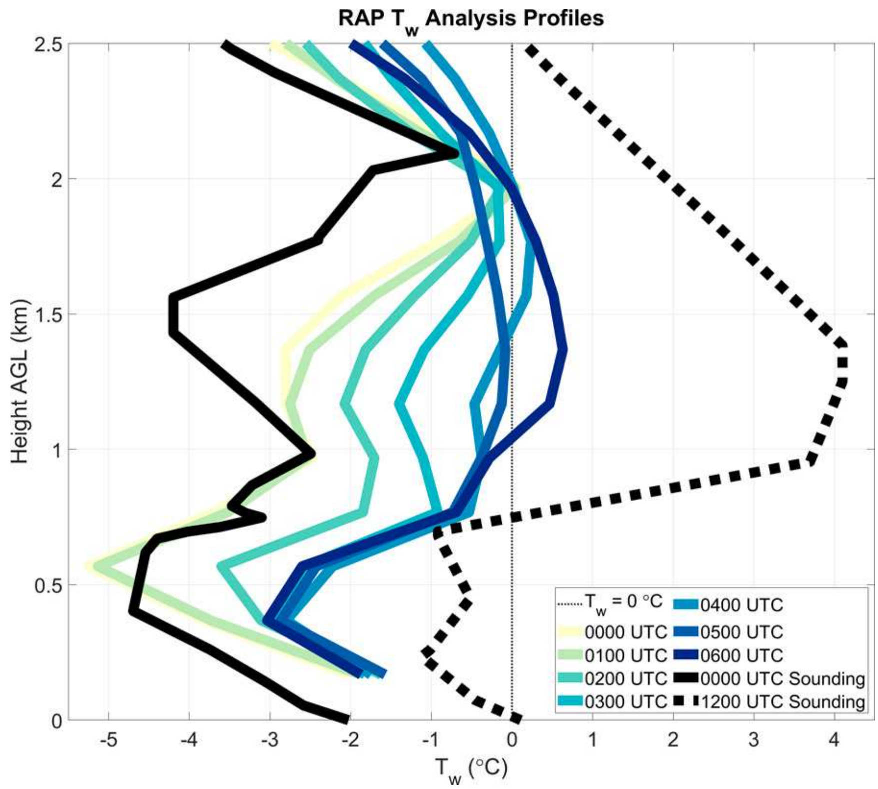

FIG. 5. Vertical profiles of wet-bulb temperature (T_w) from hourly RAP model data from 0000 to 0600 UTC (colored according to legend) 17 Dec at the model point closest to the KASPR radar. T_w profiles from the 0000 UTC (solid black) and 1200 UTC (dashed black) KOKX soundings are included.

b. *Doppler spectra at 0417 UTC: Ice-pellets-and-rain period*

KASPR QVPs summarize the polarimetric radar variable observations at 0415 UTC (Fig. 7). Melting is indicated at ~2000 m with a rapid increase in Z_H; Z_H then remains nearly constant in height toward the ground, whereas LDR steadily decreases and ρ_{hv} increases. A Z_{DR} reduction between ~1650 and 1350 m suggests the collapse of some snowflakes into liquid drops, but Z_{DR} values then remain nearly constant until ~800 m. Below 800 m, Z_H, Z_{DR}, and LDR are reduced and ρ_{hv} increases toward the surface, consistent with hydrometeor refreezing. The most drastic change in Z_H is a reduction of ~4 dB, which occurs between ~800 and 525 m. This reduction is slightly less than the theoretical 5.1 dB reduction that would be realized at Ka band for the reversion of the relative permittivity from liquid to ice particles (e.g., Ray 1972; Smith 1984; Doviak and Zrnić 1993). KASPR power measurements do not correct for hydrometeor attenuation, which may account for some of this discrepancy, in addition to not having all the liquid convert to ice, as rain is also reported at this time. Further, slight decreases in particle fall speeds increase particle concentration owing to flux conservation can lead to some additional discrepancy. Values of Z_H continue to decrease beneath this height (525 m), but the rate of change with height is reduced, indicating further, yet gradual refreezing. For comparison, KOKX raQVPs from this time are also plotted in Fig. 7. Whereas profiles within the melting layer differ owing to resonance scattering and attenuation at Ka band, and geometric differences between the radar volumes used to construct both profiles, both profiles correlate well beneath ~1300 m and capture the prominent features of interest, including enhanced Z_H and Z_{DR} values that decrease with refreezing, and reduced ρ_{hv} that increase with refreezing.

Data from the VPT scan at 0417 UTC are shown in Fig. 8. The Z_e and LDR decreases seen in the QVPs (Fig. 7) are readily apparent in the VPT scan beneath an extended depth of enhanced values between ~1800 and 625 m, which are persistent in time. LDR is thus enhanced throughout this depth at both vertical and side incidence, which indicates that particle asymmetries persist in both the horizontal and vertical planes. Melting aggregates with no preferred orientation in the horizontal plane will produce enhanced LDR values at vertical incidence (as shown in Fig. 8), provided they have a noncircular shape as viewed from below, whereas LDR is enhanced at side incidence (as shown in Fig. 7) because these particles have axis ratios that differ from unity and are thought to wobble as they fall (e.g., Ryzhkov et al. 2011; Garrett et al. 2015).

Thirty-second-averaged Doppler spectrographs at 0418 UTC (Fig. 9; frame-by-frame animation from this scan is included as online supplemental material) indicate that the melting layer

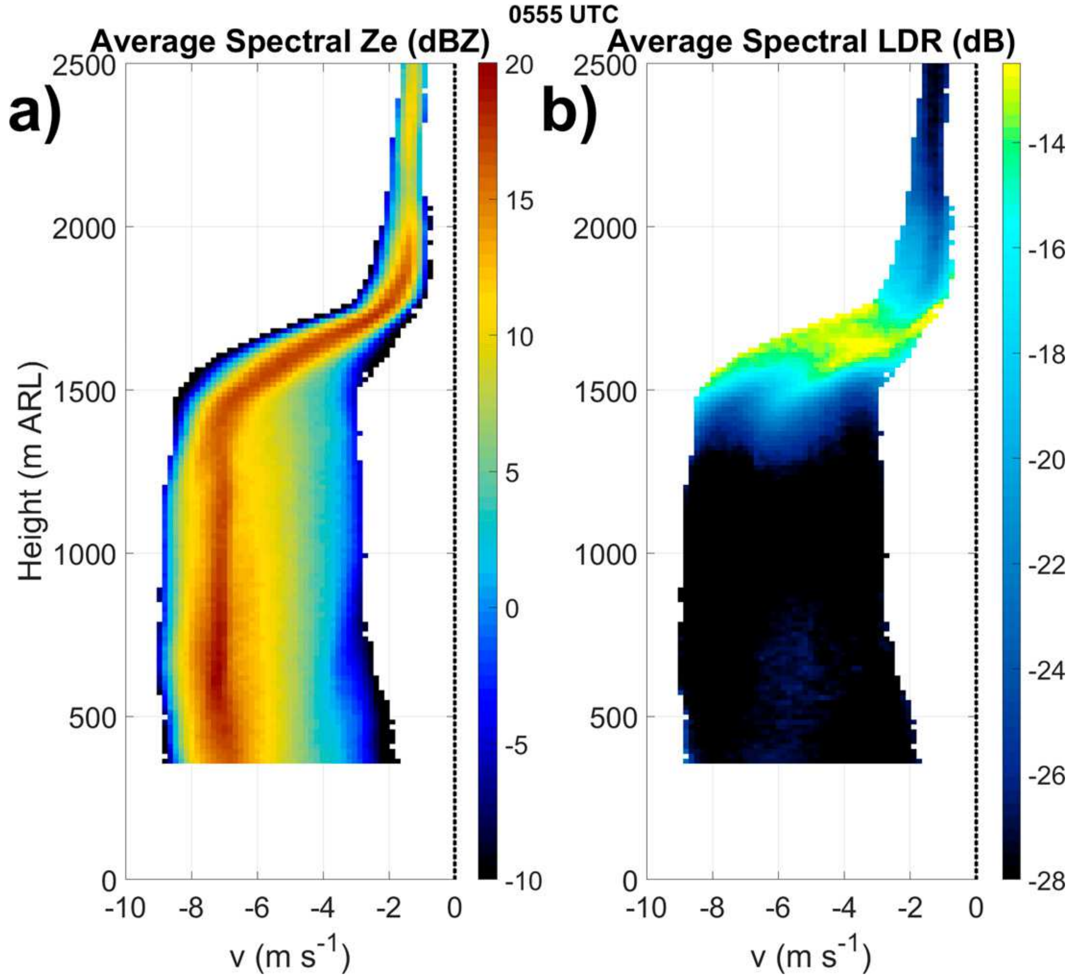

FIG. 6. Thirty-second-averaged Doppler spectrographs beginning at 0555:13 UTC of (a) spectral Z_e (in dBZ) and (b) spectral LDR (in dB) shaded according to the respective color bars. Figure 2 indicates freezing rain is reported at this time.

top is at ~1900 m, slightly lower than during the later freezing rain time. This increase in melting layer top with time is consistent with an expansion of the $T_w < 0°C$ layer for transitional cases observed by Tobin and Kumjian (2017). At 1500 m, the fastest-falling particles have reached their maximum fall speed of 7.0 m s^{-1}, which is less than the observed maximum fall speed of 8.9 m s^{-1} during the later freezing rain period (Fig. 6). Assuming that the hydrometeors falling through the $T_w < 0°C$ layer during both periods have similar characteristics, this lower maximum fall speed suggests that not all hydrometeors have melted sufficiently to have collapsed into raindrops. As a result, these partially melted, noncollapsed snowflakes retain much of their prolate or triaxial shape, and produce the observed enhanced LDR values (>−15 dB) at fall speeds lower than their collapsed counterparts.

The −18-dB LDR contour is overlaid on Fig. 9 for reference to help visually demarcate the spectral regions with enhanced LDR (>−15 dB) from those with lower LDR (<−20 dB). Between 1300 and 1000 m, this contour is nearly vertically oriented at −2.8 m s^{-1}, and both Z_e and LDR values across the spectra are nearly constant with height, denoting minimal microphysical changes to the particles within this layer. Particles with slower fall speeds to the right of the −18-dB contour have smaller LDR values, yet these values are still above the system's lower limit. Because rain is reported during this time, some of these slower-falling hydrometeors must be fully melted. However, the slightly elevated LDR suggests that these same Doppler velocity bins also contain hydrometeors that have not entirely collapsed into liquid drops and thus still contain some ice. If both liquid and noncollapsed, mixed-phase particles occupy the same Doppler velocity bin, the resulting spectral LDR in that velocity bin will be somewhere between the intrinsic value of the liquid drops (near the system's lower limit) and that of the mixed-phase particles (with higher LDR).

The questionable RAP analyses make it difficult to identify the height at which $T_w < 0°C$, and thus where refreezing of the partially melted hydrometeors begins. The VPT moments (Fig. 8) reveal a drastic Z_e reduction beginning at ~650 m, but changes in the Doppler spectra suggest that refreezing begins

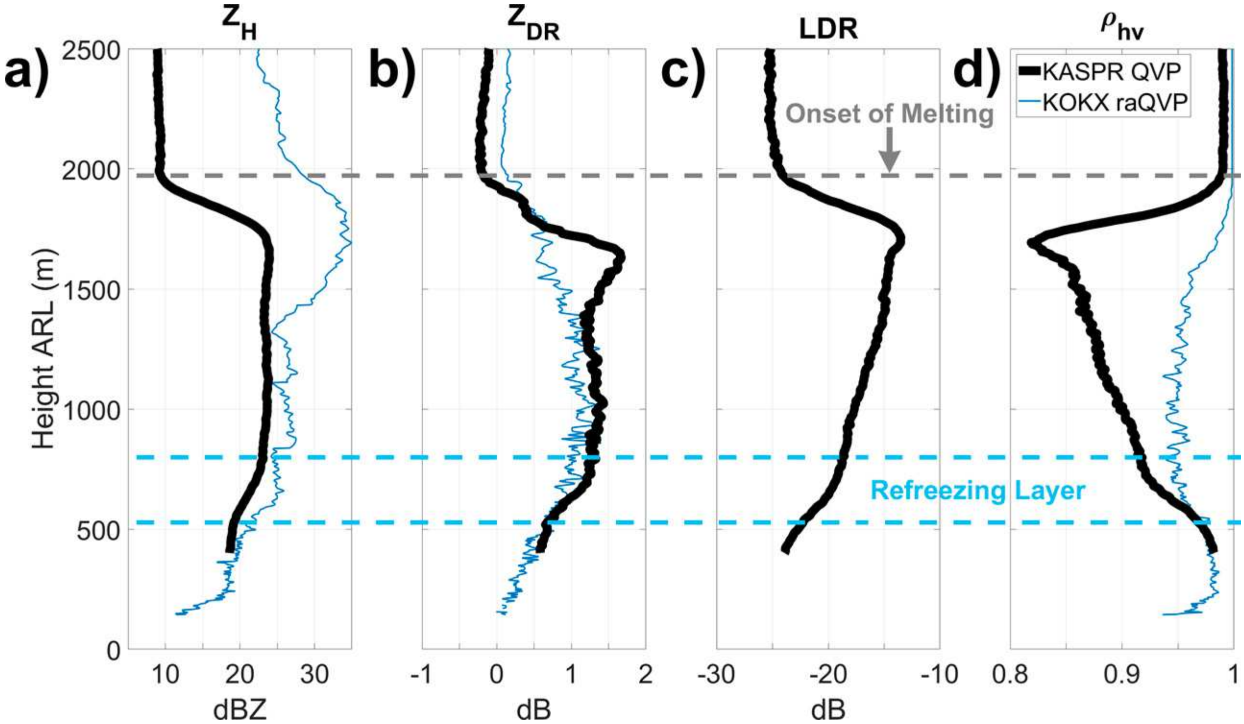

FIG. 7. KASPR QVPs (black) and KOKX raQVPs (blue) of (a) Z_H, (b) Z_{DR}, (c) LDR, and (d) ρ_{hv} at 0415 UTC. The onset of melting and the refreezing layer are annotated.

even farther aloft. An advantage of analyzing the Doppler spectra is that changes within individual velocity bins can be detected, whereas changes to the scanning polarimetric radar variables at each height are only realized when the particles dominating Z_H within the sampling volume undergo changes. There is a clear reduction in both Z_e and LDR associated with refreezing within the lowest 1000 m for particles with enhanced LDR values (>-18 dB). This is readily apparent by following the -18-dB LDR contour overlaid on both spectral Z_e and LDR from -2.8 m s^{-1} at 1000 m to decreasing velocity bins (increasing fall speeds) at lower altitudes. These changes beginning at ~1000 are ~350 m above where Z_e is more prominently reduced in the VPT scan (Fig. 8), and thus provide a better estimate of the top of the refreezing layer: the height at which *any* partially melted hydrometeor begins to refreeze. The altitude of this contour within each velocity bin correlates with heights of rapidly decreasing LDR and Z_e. These decreases in Z_e and LDR occur in the slower-falling velocity bins

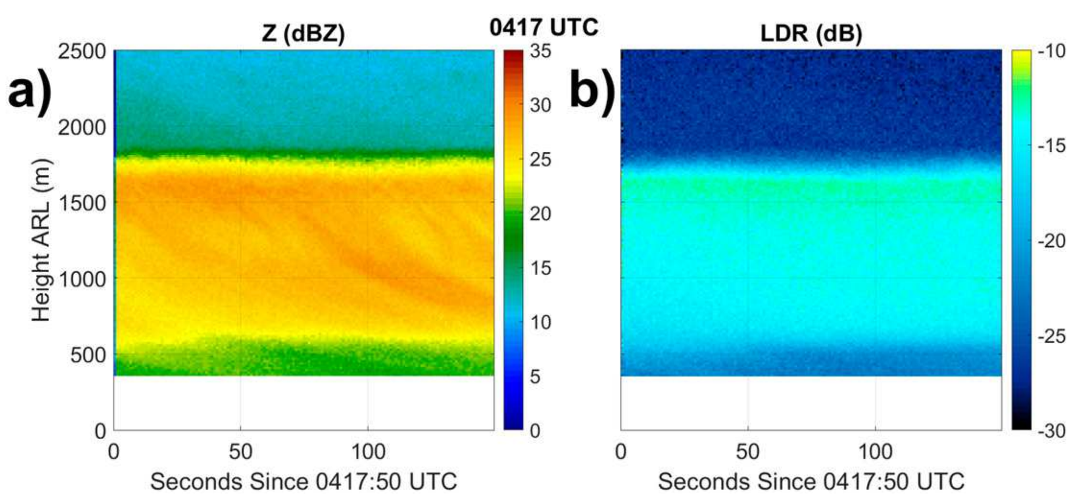

FIG. 8. Time–height depictions of (a) Z_e and (b) LDR from the KASPR vertically pointing mode beginning at 0417:50 UTC.

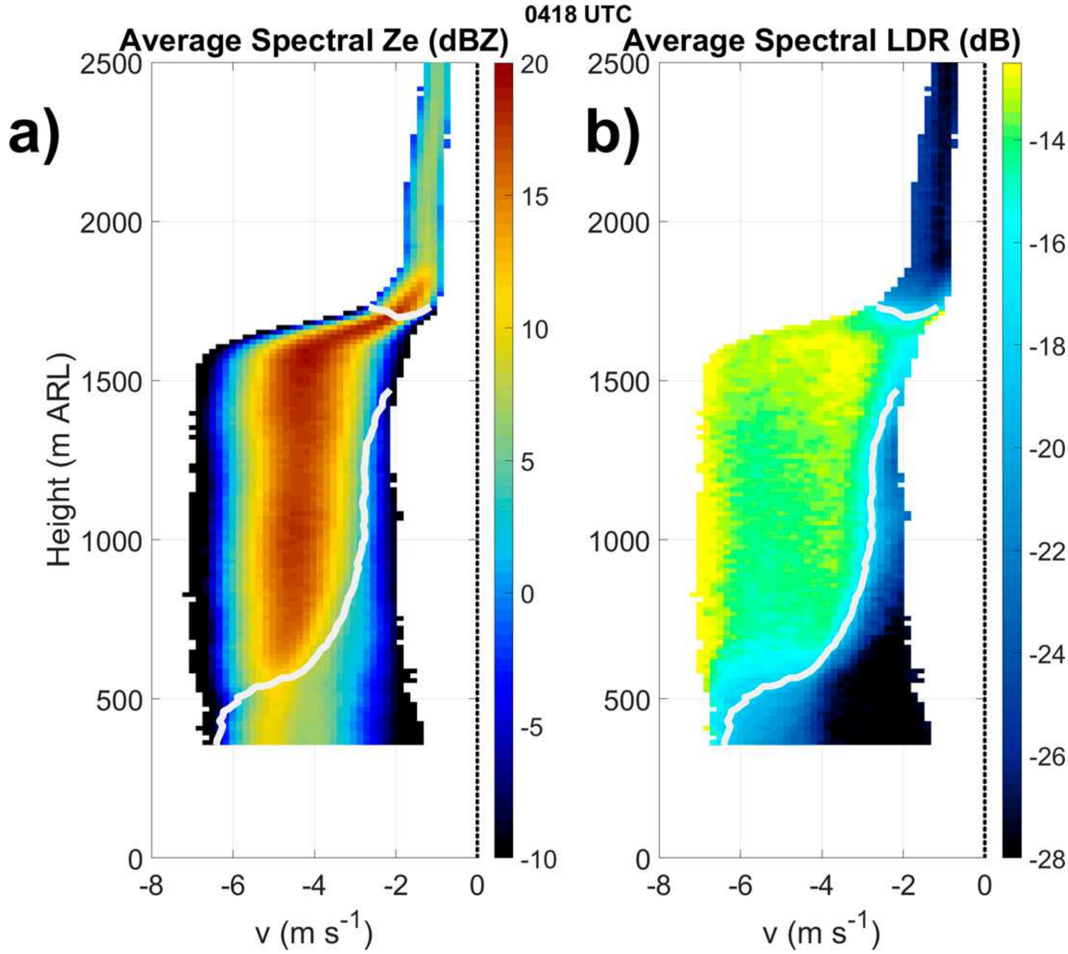

FIG. 9. Thirty-second-averaged Doppler spectrographs beginning at 0418:40 UTC of (a) spectral Z_e (in dBZ) and (b) spectral LDR (in dB) shaded according to the respective color bars. Figure 2 indicates a mixture of ice pellets and rain is reported at this time. The −18-dB LDR contour (light gray) is overlaid in both (a) and (b).

first. This is consistent with the expectation that hydrometeors with smaller liquid masses—either as the result of minimal melting aloft or small hydrometeor size—typically have lower fall speeds and require less time to completely freeze (e.g., Pruppacher and Klett 1997; Kumjian et al. 2012), and that slower-falling particles have plenty of time to freeze at greater altitudes.

No Z_{DR} enhancement was observed during this refreezing event with concurrent ice pellets and rain. Doppler spectral analysis revealed the refreezing hydrometeors in this case as partially melted and noncollapsed (i.e., particles did not reshape into raindrops) hydrometeors. This is distinct from other documented refreezing events where a Z_{DR} enhancement within the refreezing layer is present during the refreezing of fully melted hydrometeors. In light of these observations, we wish to develop a microphysical model to interrogate the polarimetric impacts of refreezing partially melted hydrometeors, in contrast to the model developed in Tobin and Kumjian (2021) that only considered the refreezing of fully melted hydrometeors.

4. Microphysical and polarimetric modeling

Polarimetric refreezing characteristics for partially melted hydrometeors have not been examined in the same manner as the refreezing of fully melted hydrometeors. Here, we develop a one-dimensional, steady-state explicit bin microphysical model to simulate the refreezing of partially melted hydrometeors. The model output is coupled to a polarimetric radar forward operator to simulate the associated radar signatures. The model isolates the first-order impact of refreezing of these particles on the polarimetric variables by accounting only for the microphysical processes of melting and refreezing. Although simulations here will use thermodynamic information from the event described in section 3, our intent is not to directly simulate the event.

a. Model description

This model is an extension of the one described in Tobin and Kumjian (2021) for the refreezing of fully melted hydrometeors. Therein, melting was not explicitly modeled, and

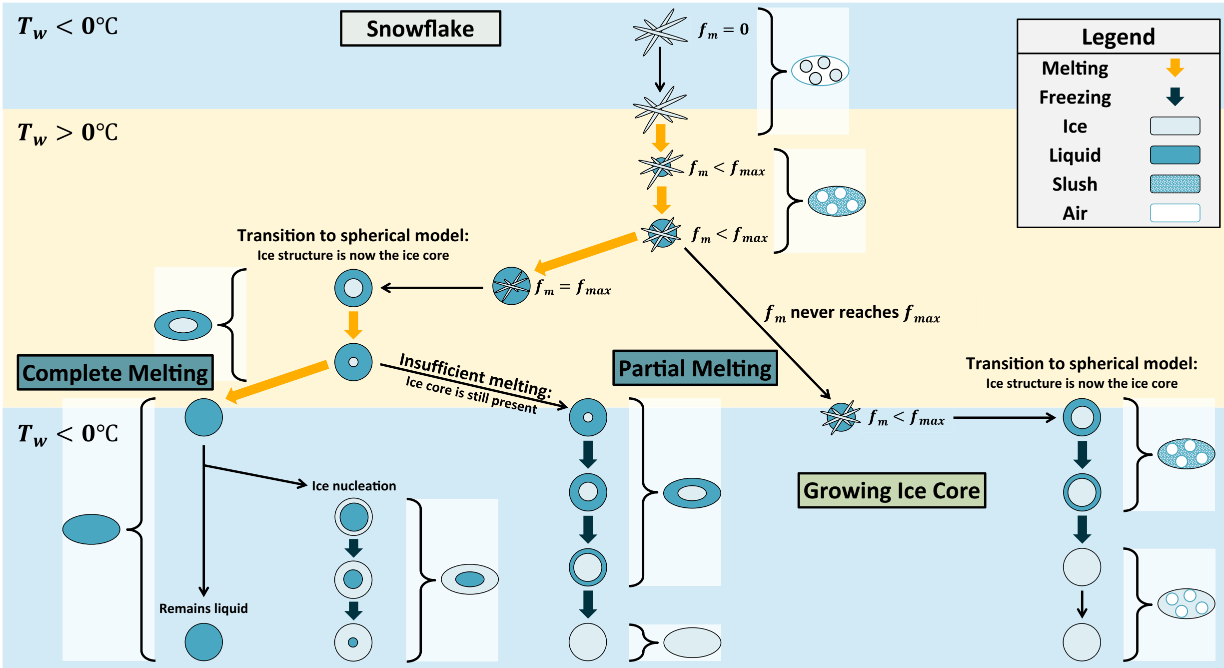

FIG. 10. Schematic of the microphysical and polarimetric model described in section 4. Melting and freezing processes, and particle composition are colored according to the legend. Beginning at the top of the diagram with the snowflake (depicted as the aggregation of four prolate ice spheroids), arrows indicate the microphysical processes and pathways possible within the microphysical model as a particle descends through the $T_w > 0$°C layer aloft and the $T_w < 0$°C near-surface layer. Particle depictions along these arrow pathways indicate how these particles are represented in the microphysical model. Particle depictions in the white boxes indicate how the polarimetric forward operator represents these particles from the microphysical model as oblate spheroids.

instead initiated with an all-liquid distribution of hydrometeors aloft. Here, melting is included to obtain a realistic distribution of partially melted hydrometeors entering the $T_w < 0$°C near-surface layer. Individual particle mass is defined by the total combined ice and liquid mass, which is conserved throughout the column within Lagrangian particle size bins. These bins are defined as the equivalent-volume diameter of a solid ice pellet in 0.1-mm increments from 0.1 to 4.0 mm, consistent with both simulations in Tobin and Kumjian (2021) and the maximum particle dimension of 3.8 mm inferred by the Doppler spectral data in section 3. We retain mass exchange with the environment (evaporation–condensation, sublimation–deposition) only in the thermal energy balance equations, and ignore particle interactions such as riming, collisions, aggregation, and breakup. We refer the reader to Tobin and Kumjian (2021) for a more detailed description of the model. Here, the modifications implemented to account for melting are described.

The model assumes a thermodynamic profile characteristic of ice pellets and/or freezing rain with a single elevated layer of $T_w > 0$°C above a near-surface $T_w < 0$°C layer (e.g., Brooks 1920; Hanesiak and Stewart 1995; Zerr 1997). Here, we initialize the model using the 0600 UTC RAP profile (Fig. 5). We choose the 0600 UTC profile instead of 0400 UTC to obtain a more realistic representation of liquid water mass fraction f_m across our distribution that corresponds well with our analysis in section 3b. The two profiles are otherwise similar below 1000 m where hydrometeor refreezing occurs.

A schematic of the various pathways an individual particle can take within the microphysical model is shown in Fig. 10. All particles begin as dry snowflakes in the $T_w < 0$°C layer aloft, and then begin to melt within the $T_w > 0$°C layer. Snowflakes are modeled in accordance with Szyrmer and Zawadzki (1999), who provide equations of f_m for melting snowflakes and the critical value at which the remaining ice structure is completely embedded within the meltwater (f_{max}; i.e., the point where snowflakes have collapsed into raindrops and can no longer be modeled as snowflakes). The size and density of these snowflakes, however, is modified to follow expressions in Carlin and Ryzhkov (2019) for unrimed snowflakes. Using this approximation, particles in the 4.0-mm bin originate as 16.2-mm diameter snowflakes aloft, and particles in the 1.0 mm bin originate as 2.2-mm diameter snowflakes aloft. We modify an assumption in Carlin and Ryzhkov (2019) by relaxing the maximum allowable snowflake density from 500 kg m^{-3} to that of ice (917 kg m^{-3}). This change allows a seamless transition from melting snowflakes to melting and/or refreezing ice spheres, as will be discussed presently.

Snowflakes that have reached f_{max} can no longer be modeled following Szyrmer and Zawadzki (1999), as ice is no longer assumed to protrude from the meltwater. At this point, the remaining ice structure is converted into a spherical ice core, and the meltwater is evenly distributed around the particle's exterior. This assumption necessitates the relaxation of the maximum allowable snowflake density in Carlin and Ryzhkov (2019) to remove air from these melting snowflakes. Conversion to a solid ice core allows further particle melting to follow the idealized melting of an ice sphere theorized by Mason (1956) and further elaborated on in Pruppacher and Klett (1997). These relations assume no circulations within the meltwater, and that both the ice–liquid interface and particle surface temperature are at the triple point temperature of water ($T_0 = 273.15$ K). The steady-state, radially symmetric thermal energy balance expression thus equates the rate of enthalpy uptake via melting with the energy transfer through the air and the rate of evaporation/condensation.

If particles melt completely (i.e., $f_m = 1$) within the elevated $T_w > 0°C$ layer, we assume that they remain as liquid drops through the remainder of the column. Although these drops are supercooled within the $T_w < 0°C$ near-surface layer, they do not refreeze because the $-2.8°C$ minimum T_w within this layer does not meet the $T_w \leq -5°C$ threshold typically chosen to initiate freezing of these drops (e.g., Reeves et al. 2016; Ryzhkov and Zrnić 2019; Tobin and Kumjian 2021). If, however, collapsed snowflakes do not melt completely (i.e., $f_{max} < f_m < 1$), refreezing commences within the $T_w < 0°C$ near-surface layer in accordance with the same thermal energy balance equations and assumptions used for melting an ice sphere (i.e., refreezing progresses radially outward from a growing ice core). If melting snowflakes do not reach their f_{max} prior to encountering the $T_w < 0°C$ near-surface layer, the remaining ice structure of these noncollapsed snowflakes is transitioned into a spherical ice core, and refreezing progresses in the same manner as for the partially melted, collapsed snowflakes. Although this is not physically consistent with how such particles refreeze in nature, this assumption provides a simple estimation of f_m with refreezing. In reality, such partially melted snowflakes would refreeze at the ice–liquid interface of the embedded ice structure.

The microphysical model is coupled to the polarimetric radar forward operator discussed in Ryzhkov et al. (2011). We assume particles are oblate spheroids, and follow the equations for a low radar elevation angle where hydrometeors assumed to have a two-dimensional axisymmetric Gaussian distribution of canting angles with a mean of 0°. We simulate polarimetric radar profiles at both S band (11.0 cm) and Ka band (8.5 mm). For S band, we use the small-particle scattering approximation, which is valid for the particles considered here. For Ka band, scattering amplitudes are calculated from the T-matrix method for two-layer spheroids (Bringi and Seliga 1977a,b; Mishchenko 2000).

Alongside how particles are depicted in the microphysical model, Fig. 10 shows how the various particle types are depicted in the polarimetric radar model. We take the approach discussed in Carlin and Ryzhkov (2019)—where snowflakes are modeled simply as homogeneous three-phase spheroids with evenly distributed spherical inclusions of ice, air, and liquid—and apply it to all noncollapsed snowflakes, both melting and refreezing. For the refreezing of noncollapsed snowflakes, we assume that the volume of air within the particle and the particle's axis ratio both remain constant at their respective values from when they first encounter the $T_w < 0°C$ near-surface layer. This "corrects" for the nonphysical assumption of the microphysical model to convert the remaining ice structure into an ice core and remove air from these particles. Collapsed snowflakes are modeled as either two-layer spheroids with an ice core and liquid exterior, or as one-layer liquid or ice spheroids depending on f_m. For simplicity, we follow the assumptions in Ryzhkov et al. (2011) and Kumjian et al. (2012) where the inner spheroid axis ratios are equivalent to that of the exterior of the particle, and that the canting angle distribution width is set to 10° for raindrops and 40° for ice pellets. Regardless of particle type, we assume that the particle temperature is at T_0 if the particle has both liquid and ice masses, but otherwise assume that the particle temperature has adjusted to the ambient temperature.

Via the steady-state approximation, flux is conserved within each particle bin throughout the column as the product of particle fall speed and number concentration. Following Tobin and Kumjian (2021), this flux is calculated for solid ice pellets at the surface using the ice pellet fall speed expression in Kumjian et al. (2012) and the gamma distribution of ice pellet major axis lengths in Gibson et al. (2009) for the 17 January 2006 ice pellet event in Montreal, Quebec. Particle fall speeds for all collapsed snowflake particles (i.e., liquid drops, liquid-coated ice spheres, and ice pellets) follow from Kumjian et al. (2012). Fall speeds for melting, noncollapsed snowflakes follow from relations in Szyrmer and Zawadzki (1999) where fall speeds vary linearly between snow and rain based on f_m. For refreezing, noncollapsed snowflakes, the fall speed is computed using the maximum f_m value attained by the snowflakes during melting, because we expect insignificant fall speed changes from these particles in nature owing to minimal particle shape and size changes upon refreezing.

This model has several limitations owing to its simplified nature. Whereas more complex and complete microphysical models exist for melting and freezing (e.g., Khain et al. 2011; Phillips et al. 2014, 2015; Ilotoviz et al. 2016), this model isolates the first-order impacts of these processes on the polarimetric radar variables by removing any confounding effects of particle interactions or breakup. Further, our treatment of melting and refreezing snowflakes is highly idealized, and more-realistic simulations would require more complex thermodynamic equations and scattering models to account for the complex geometries of such particles (e.g., Leinonen and von Lerber 2018).

b. Model results

Resulting f_m values for the simulation are shown in Fig. 11. Particles with an ice pellet equivalent volume diameter < 1.9 mm are fully melted, and those with a binned diameter ≥ 2.0 mm never reached their respective f_{max} values (not shown). Particles begin to melt at 1960 m, with the smallest particles collapsing and melting completely over a very shallow depth. Refreezing of the partially melted hydrometeors begins at 1010 m. The smallest of the non–completely melted hydrometeors (1.9-mm binned diameter) achieve a maximum f_m of 0.97, whereas the largest hydrometeors (4.0-mm binned diameter) achieve a maximum f_m of 0.36. Whereas the smaller non–completely melted hydrometeors do

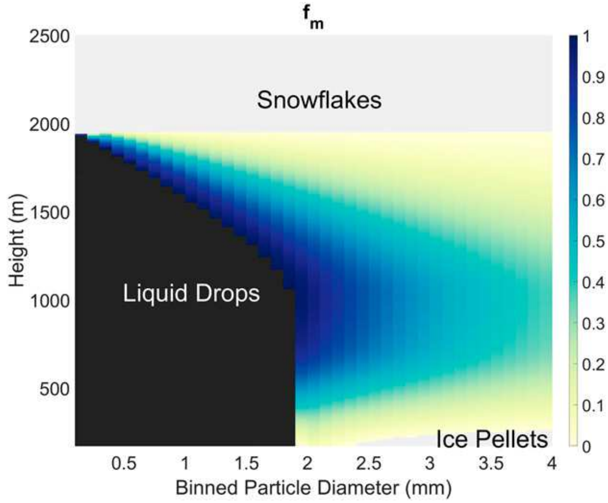

FIG. 11. Liquid water mass fraction (f_m; shaded according to color bar) of simulated hydrometeors falling through the assumed thermodynamic profile from the 0600 UTC RAP sounding on 17 Dec at the model point closest to the KASPR (Fig. 5). Dark gray indicates that hydrometeors are liquid drops, and light gray indicates dry snowflakes (aloft) or solid ice pellets (near the surface).

not refreeze completely by 170 m (the lowest level in the simulation), the largest hydrometeors refreeze completely by 260 m.

Simulated vertical profiles of S- and Ka-band Z_H, Z_{DR}, LDR, and ρ_{hv} are shown in Fig. 12, excluding any effects of attenuation. Owing to our simplified treatment of melting snowflakes aloft, and our aim to model refreezing as opposed to melting, we focus this analysis on the simulated polarimetric radar variables within the refreezing layer (below 1010 m). S-band profiles adequately capture the observed refreezing characteristics of gradual reductions in Z_H, Z_{DR}, and LDR, and an increase in ρ_{hv}. Ka-band Z_H also produces a gradual Z_H reduction, yet Z_H at the top of the refreezing layer is 9.7 dB lower than at S band. We attribute this difference to resonance scattering effects at Ka band for the large, wetted snowflakes. Resonance scattering effects at Ka band for liquid particles begins at ~2.5 mm. Because particles with binned sizes ≥ 2.0 mm do not collapse into raindrops, they are even larger and wetted particles, so resonance scattering effects will be prominent at Ka band. Further, our assumptions of spheroidal particle geometry maximize resonance scattering effects, whereas irregular shapes observed within nature tend to destroy some of those near-field interactions. These modeled resonance scattering effects propagate into Z_{DR}, LDR, and ρ_{hv} observations above ~500 m where values of Z_{DR} and LDR are lower than expected, and ρ_{hv} values are higher than expected. Below 500 m, the Ka-band profiles are consistent with observations with decreasing Z_{DR} and LDR values, and increasing ρ_{hv} values toward the ground.

We note that Z_H in our S-band simulations are 10 dB higher than observations (Fig. 7) owing to our treatment of snowflakes and assumed particle size distribution, and that our simulations were not constrained using observations. Z_H for the Ka-band simulation, on the other hand, corresponds rather well to observations and are only ~5 dB higher. We attribute this difference to a combination of resonance scattering

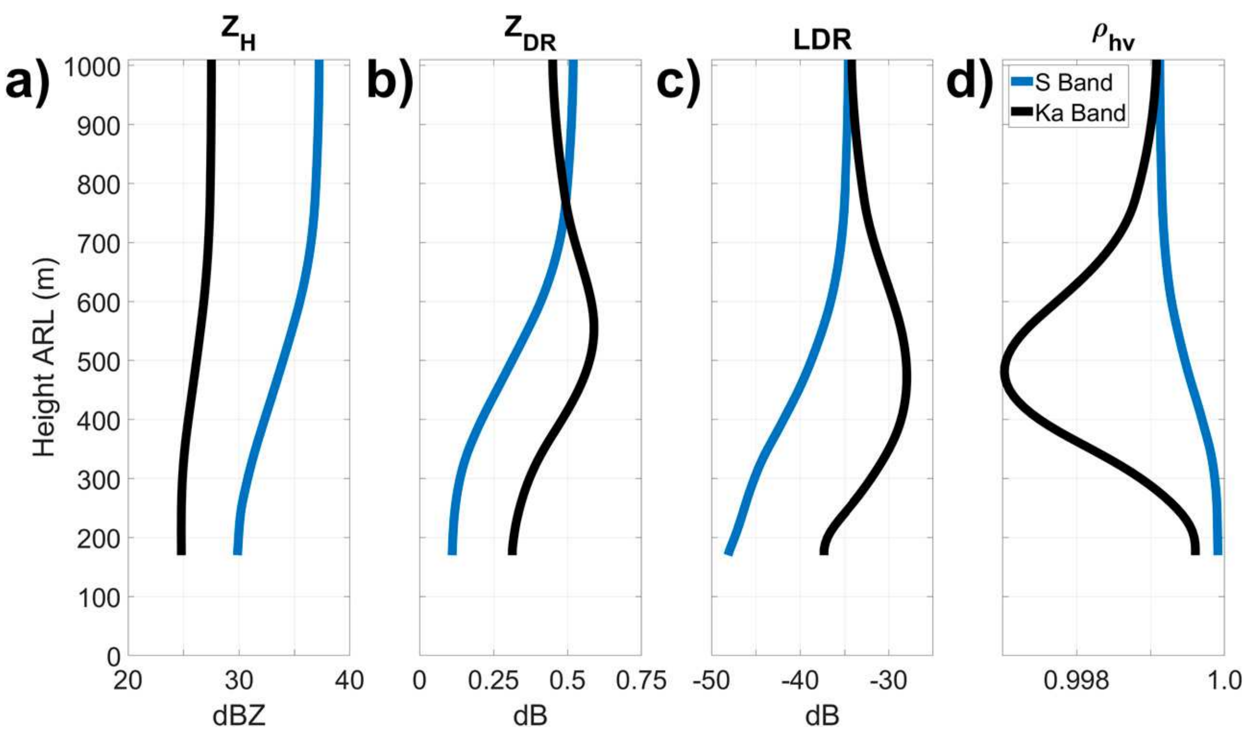

FIG. 12. Simulated vertical profiles of (a) Z_H, (b) Z_{DR}, (c) LDR, and (d) ρ_{hv} at S band (blue) and Ka band (black).

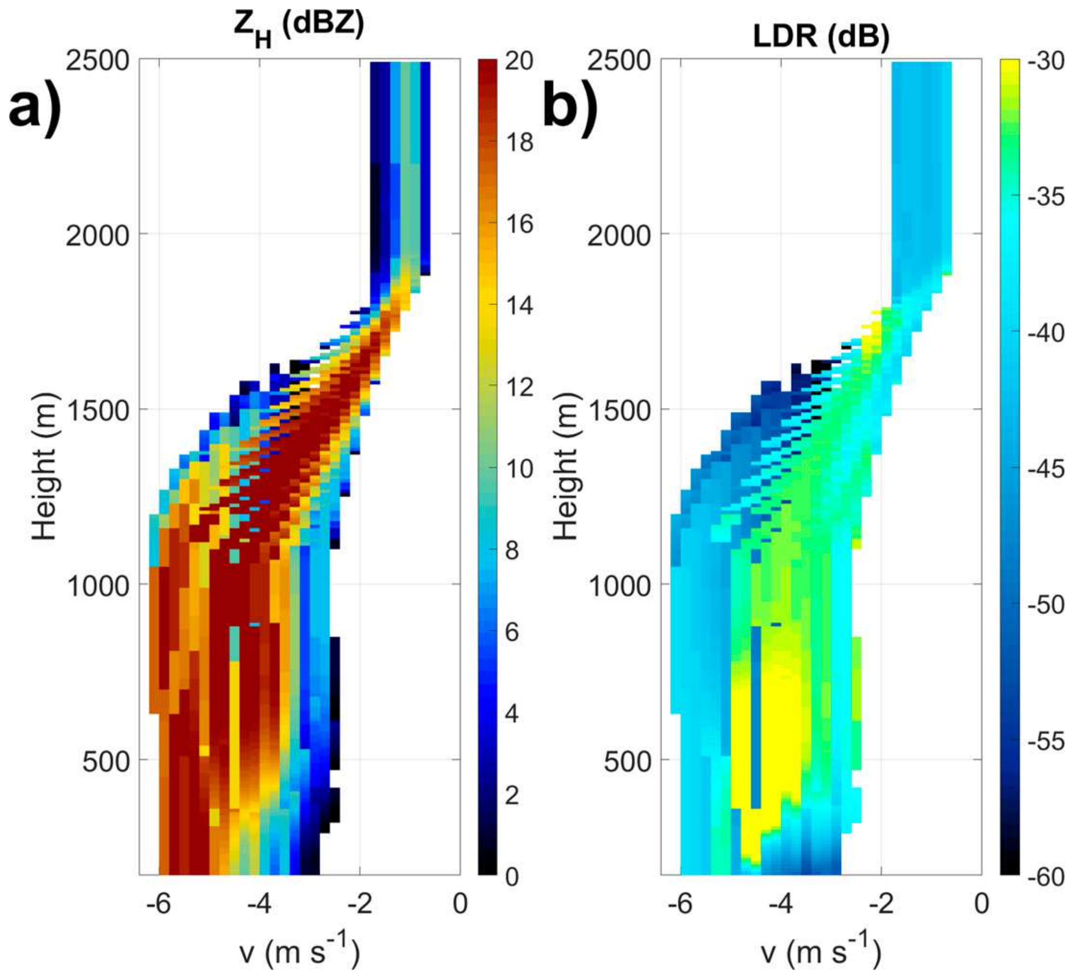

FIG. 13. Simulated Doppler spectrographs at side incidence of (a) spectral Z_e (in dBZ) and (b) spectral LDR (in dB) shaded according to the respective color bars.

effects in the simulation and attenuation in the KASPR observations. Z_{DR} values are lower than observed for both radars, and LDR is significantly lower than observed from KASPR, which we attribute to our simplified geometry of hydrometeors as oblate spheroids, particularly for snowflakes. Last, ρ_{hv} values are significantly higher in our simulations, again owing to our simplified geometries and lack of any ground clutter that may negatively bias ρ_{hv} in the observations.

In addition to vertical polarimetric radar profiles, Doppler spectra can also be simulated with the model to compare against observations. However, because hydrometeors are modeled as oblate spheroids, which have LDR = $-\infty$ dB as viewed from below, our simulated Doppler spectra will be for Z_H and LDR at side incidence. Because the major axis of an oblate spheroid is the same as viewed from the side as from below, spectral Z_H values will be similar for both orientations. Observations reveal that the particles with elevated LDR values as viewed from below (i.e., wetted, noncollapsed snowflakes; Figs. 6, 8, 9) also have elevated LDR values at side incidence (Figs. 4, 7). We argue that these particles within our simulations will have elevated LDR values compared to smaller collapsed snowflakes and raindrops owing to the lower axis ratios and increased canting angle distribution width chosen for snowflakes.

Simulated Doppler spectrographs of Z_H and LDR at side incidence within 0.2 m s^{-1} velocity bins are shown in Fig. 13. Velocity bins with spectral $Z_H < 0$ dBZ are filtered for clarity. Melting within these spectrographs are consistent with observations in terms of increased Z_H and LDR values beginning at 1900 m, followed by subsequent increases in particle fall speeds. Hydrometeors reach a maximum fall speed of 6.2 m s^{-1} at 1200 m, which is lower than the 7.0 m s^{-1} fall speeds attained at ~1500 m in Fig. 9. This suggests that the model does not melt hydrometeors as quickly as observed, likely owing in part to the cold bias suspected in the RAP profiles for this event used to initialize the model. Nevertheless, the model produces enhanced Z_H and LDR values beneath 1100 m primarily in the 3.0–5.0 m s^{-1} velocity bins, which correspond well with observations. We also note decreases in Z_H and LDR with refreezing that occur within the slower-falling particle bins first, similar to observations. These changes are most pronounced below 550 m.

Both the microphysical and polarimetric simulations are qualitatively consistent with observations. The model successfully melts small hydrometeors completely, whereas larger hydrometeors do not melt sufficiently to collapse into raindrop shapes, and thus refreeze within the $T_w < 0°C$ near-surface layer. Further, the model produces neither a Z_{DR} nor LDR enhancement within the refreezing layer, with the exception of the Ka-band profile where the reduced values aloft are the result of resonance scattering effects. Instead, Z_H, Z_{DR}, and LDR values remain enhanced alongside low ρ_{hv} values beneath the melting layer, with gradual changes to each variable as the hydrometeors freeze. Interestingly, the layer in which the model produces more drastic polarimetric changes (770–570 m) corresponds well with the layer in which the KASPR QVP observations indicate drastic changes associated with refreezing (800–525 m; Fig. 7). Again, it is unclear the exact height at which refreezing initiates in the observations, owing to questionable RAP profiles during the event and a lack of in situ thermodynamic observations. However, if the 0600 UTC RAP profiles are reasonably accurate for the observations at 0417 UTC, it suggests that the microphysical model successfully replicates refreezing and the corresponding shape of the polarimetric profiles at this time, including the height at which all partially melted hydrometeors have fully refrozen. Refreezing initiates at a higher altitude in the model (1450 m) than indicated by the Doppler spectral data observations (~1000 m; Fig. 9).

5. Summary and discussion

The polarimetric refreezing signature—indicative of hydrometeor refreezing—has been documented in the literature as a distinct enhancement in differential reflectivity (Z_{DR}) within a region of decreasing radar reflectivity (Z_H) toward the ground. A long-duration ice-pellets-and-rain mixture case on 17 December 2019 over central Long Island was examined using data from two radars: the Ka-band KASPR research radar, and the S-band KOKX operational radar. KASPR provides higher-resolution data than KOKX, and measurements of linear depolarization ratio (LDR) and Doppler spectral data collected at vertical incidence. KOKX, on the other hand, provides data consistent with operational radars across the United States. The use of both radars affords greater insights into the microphysical processes responsible for the refreezing signature, while allowing the findings to be applicable to operational radars.

Unlike previously documented refreezing events, no characteristic Z_{DR} enhancement was produced for either radar. Instead, observed features include reductions in Z_H, Z_{DR}, and LDR toward the surface, whereas ρ_{hv} increases as freezing progresses. Doppler spectral data featured enhanced spectral LDR values, indicating that many hydrometeors did not collapse into raindrop shapes within the $T_w > 0°C$ layer, and thus did not completely melt prior to refreezing. This is distinct from previously documented cases where particles were fully melted prior to refreezing. Smaller-massed particles that completely melted aloft did not nucleate ice within the $T_w < 0°C$ near-surface layer, and instead remained as liquid drops, corresponding with rain observations at the surface.

A microphysical model was developed and coupled to a polarimetric radar forward operator to further document the polarimetric features of partially melted hydrometeor refreezing. The model successfully produced partially melted, noncollapsed larger hydrometeors and fully melted smaller hydrometeors, and replicated features of the observed polarimetric profiles and Doppler spectra. Refreezing in S-band simulations produced reductions in Z_H, Z_{DR}, and LDR, and ρ_{hv} increases. Resonance scattering effects in the Ka-band simulations contributed to slight increases in Z_{DR} and LDR aloft before their respective reductions toward the ground, and corresponding decreases in ρ_{hv} before increasing. Such effects were not as prominent in observations owing to the complex geometries of particles found in nature that can mitigate resonance scattering effects. Simulated Doppler spectra at Ka band reveal enhanced LDR values consistent with observations to indicate partially melted, noncollapsed snowflakes. Although the simulated Doppler spectra are a crude approximation based on the limitations of our microphysical model, the concept can be applied in future studies for more complex models with additional processes such as riming and aggregation.

These observations and modeling efforts show that the refreezing of partially melted hydrometeors results in a single layer of enhanced Z_H, Z_{DR}, and LDR with corresponding reductions in ρ_{hv} associated with both melting and refreezing, as opposed to two discrete layers (i.e., a melting and a refreezing layer) separated by an intermediate layer of liquid hydrometeors, as observed in the refreezing of fully melted hydrometeors (e.g., Kumjian et al. 2013, 2020; Ryzhkov et al. 2016; Van Den Broeke et al. 2016; Tobin and Kumjian 2017, 2021). As a result, ρ_{hv} actually *increases* with refreezing toward the surface. This is distinct from the localized ρ_{hv} reduction seen for the refreezing of fully melted hydrometeors where values are initially very high in the overlying layer of fully melted hydrometeors, and reduced where refreezing occurs (e.g., Kumjian et al. 2013; Tobin and Kumjian 2021).

We contrast our results with recent modeling efforts in Tobin and Kumjian (2021), wherein the formation of an overly oblate unfrozen region within freezing particles is theorized as the reason behind the Z_{DR} enhancement of the refreezing signature. Further, *no* Z_{DR} *enhancement* was produced *without* the overly oblate unfrozen core. Instead, a Z_{DR} reduction was produced owing to the reversion of hydrometeor relative permittivity from liquid to ice. Here, partially melted hydrometeors did not form an ice shell upon refreezing, as the existing ice structure embedded within the particles instead serves as ideal sites for ice growth. Instead, the reductions in Z_{DR} resulted from the change in relative permittivity of an ice-and-liquid hydrometeor to an ice hydrometeor with freezing. *Thus, we suggest that the presence or absence of an asymmetric unfrozen region within an ice shell as the reason for the disparate refreezing signatures for fully and partially melted hydrometeors.* In the absence of such particle geometry, reductions in Z_{DR} are instead observed.

It was previously thought that, perhaps, the Z_{DR} enhancement was associated with hydrometeor refreezing in general. However, these new results suggest that the enhancement *is not associated* with the refreezing of partially melted hydrometeors. Additional observations and studies are required to determine whether all cases of completely melted hydrometeor refreezing produce a Z_{DR} enhancement, and whether no cases of partially melted hydrometeor refreezing produce a Z_{DR} enhancement. However, if this distinction holds true, where a Z_{DR} enhancement is only produced for fully melted hydrometeors, the presence or absence of the enhancement during ice pellet events can provide valuable information about near-surface hydrometeor species. For example, if ice pellets are reported at the surface yet no Z_{DR} enhancement is present, particles begin refreezing at $T_w = 0°C$. If the signature is present, however, it could indicate the presence of a supercooled liquid drop layer where fully melted particles aloft do not nucleate ice until lower temperatures closer to the surface. As supercooled liquid drops are hazardous to aviation, it is crucially important to identify and distinguish these two ice pellet formation types, and polarimetric radar observations may be useful for such winter-precipitation applications.

Acknowledgments. We thank Drs. E. Clothiaux and J. Harrington (Penn State) for their helpful comments and suggestions. PK and MO contributions were supported by NSF AGS Grant 1841215.

Data availability statement. ASOS data were obtained from Iowa Environmental Mesonet at https://mesonet.agron.iastate.edu/request/download.phtml. RAP and KOKX radar data were obtained from National Centers for Environmental Information at https://www.ncei.noaa.gov/has/HAS.DsSelect. KASPR radar data used in this study are available at the Stony Brook University Academic Commons.

REFERENCES

Bendel, W. B., and D. Paton, 1981: A review of the effect of ice storms on the power industry. *J. Appl. Meteor. Climatol.*, **20**, 1445–1449, https://doi.org/10.1175/1520-0450(1981)020<1445:AROTEO>2.0.CO;2.

Benjamin, S. G., and Coauthors, 2016: A North American hourly assimilation and model forecast cycle: The Rapid Refresh. *Mon. Wea. Rev.*, **144**, 1669–1694, https://doi.org/10.1175/MWR-D-15-0242.1.

Bennett, I., 1959: Glaze: Its meteorology and climatology, geographical distribution and economic effects. Environmental Protection Research Division Tech. Rep. EP-105, 217 pp.

Bernabó, P., F. Cuccoli, L. Baldini, and V. Chandrasekar, 2016: Super-cooled liquid water droplets detection using dual-polarization radar. *2016 IEEE Metrology for Aerospace*, Florence, Italy, IEEE, 118–123, https://doi.org/10.1109/MetroAeroSpace.2016.7573197.

Brandes, E. A., G. Zhang, and J. Vivekanandan, 2002: Experiments in rainfall estimation with a polarimetric radar in a subtropical environment. *J. Appl. Meteor.*, **41**, 674–685, https://doi.org/10.1175/1520-0450(2002)041<0674:EIREWA>2.0.CO;2.

Bringi, V. N., and T. A. Seliga, 1977a: Scattering from axisymmetric dielectrics or perfect conductors imbedded in an axisymmetric dielectric. *IEEE Trans. Antennas Propag.*, **25**, 575–580, https://doi.org/10.1109/TAP.1977.1141642.

——, and ——, 1977b: Scattering from nonspherical hydrometeors. *Ann. Telecommun.*, **32**, 392–397, https://doi.org/10.1007/BF03003484.

Brooks, C. F., 1920: The nature of sleet and how it is formed. *Mon. Wea. Rev.*, **48**, 69–72, https://doi.org/10.1175/1520-0493(1920)48<69b:TNOSAH>2.0.CO;2.

Carlin, J. T., and A. V. Ryzhkov, 2019: Estimation of melting-layer cooling rate from dual-polarization radar: Spectral bin model simulations. *J. Appl. Meteor. Climatol.*, **58**, 1485–1508, https://doi.org/10.1175/JAMC-D-18-0343.1.

Changnon, S. A., 2003: Characteristics of ice storms in the United States. *J. Appl. Meteor. Climatol.*, **42**, 630–639, https://doi.org/10.1175/1520-0450(2003)042<0630:COISIT>2.0.CO;2.

DiVito, S., and J. T. Riley, 2017: An overview of the Federal Aviation Administration (FAA) Terminal Area Icing Weather Information for NextGen (TAIWIN) project. *18th Conf. on Aviation, Range, and Aerospace Meteorology*, Seattle, WA, Amer. Meteor. Soc., 7.1, https://ams.confex.com/ams/97Annual/webprogram/Paper314380.html.

Doviak, R. J., and D. S. Zrnić, 1993: *Doppler Radar and Weather Observations*. 2nd ed. Academic Press, 562 pp.

Dunnavan, E. L., Z. Jiang, J. Y. Harrington, J. Verlinde, K. Fitch, and T. J. Garrett, 2019: The shape and density evolution of snow aggregates. *J. Atmos. Sci.*, **76**, 3919–3940, https://doi.org/10.1175/JAS-D-19-0066.1.

FAA, 1995: Aviation safety action plan: Zero accidents: A shared responsibility. Federal Aviation Administration Rep., 69 pp., https://apps.dtic.mil/dtic/tr/fulltext/u2/a307192.pdf.

Garrett, T. J., S. E. Yuter, C. Fallgatter, K. Shkurko, S. R. Rhodes, and J. L. Endries, 2015: Orientations and aspect ratios of falling snow. *Geophys. Res. Lett.*, **42**, 4617–4622, https://doi.org/10.1002/2015GL064040.

Gibson, S. R., and R. E. Stewart, 2007: Observations of ice pellets during a winter storm. *Atmos. Res.*, **85**, 64–76, https://doi.org/10.1016/j.atmosres.2006.11.004.

——, ——, and W. Henson, 2009: On the variation of ice pellet characteristics. *J. Geophys. Res.*, **114**, D09207, https://doi.org/10.1029/2008JD011260.

Green, S. D., 2015: The Icemaster Database and an analysis of aircraft aerodynamic icing accidents and incidents. FAA Rep. DOT/FAA/TC-14/44, 135 pp., http://www.tc.faa.gov/its/worldpac/techrpt/tc14-44.pdf.

Griffin, E. M., T. J. Schuur, A. V. Ryzhkov, H. D. Reeves, and J. C. Picca, 2014: A polarimetric and microphysical investigation of the northeast blizzard of 8–9 February 2013. *Wea. Forecasting*, **29**, 1271–1294, https://doi.org/10.1175/WAF-D-14-00056.1.

Hanesiak, J. M., and R. E. Stewart, 1995: The mesoscale and microscale structure of a severe ice pellet storm. *Mon. Wea. Rev.*, **123**, 3144–3162, https://doi.org/10.1175/1520-0493(1995)123<3144:TMAMSO>2.0.CO;2.

Hogan, R. J., L. Tian, P. R. A. Brown, C. D. Westbrook, A. J. Heymsfield, and J. D. Eastment, 2012: Radar scattering from ice aggregates using the horizontally aligned oblate spheroid approximation. *J. Appl. Meteor. Climatol.*, **51**, 655–671, https://doi.org/10.1175/JAMC-D-11-074.1.

Ilotoviz, E., A. P. Khain, N. Benmoshe, V. T. J. Phillips, and A. V. Ryzhkov, 2016: Effect of aerosols on freezing drops, hail, and precipitation in a midlatitude storm. *J. Atmos. Sci.*, **73**, 109–144, https://doi.org/10.1175/JAS-D-14-0155.1.

Jiang, Z., J. Verlinde, E. E. Clothiaux, K. Aydin, and C. Schmitt, 2019: Shapes and fall orientations of ice particle aggregates. *J. Atmos. Sci.*, **76**, 1903–1916, https://doi.org/10.1175/JAS-D-18-0251.1.

Kennedy, P. C., and S. A. Rutledge, 2011: S-band dual-polarization radar observations of winter storms. *J. Appl. Meteor. Climatol.*, **50**, 844–858, https://doi.org/10.1175/2010JAMC2558.1.

Khain, A. P., D. Rosenfeld, A. Pokrovsky, U. Blahak, and A. Ryzhkov, 2011: The role of CCN in precipitation and hail in a midlatitude storm as seen in simulations using a spectral (bin) microphysics model in a 2D dynamic frame. *Atmos. Res.*, **99**, 129–146, https://doi.org/10.1016/j.atmosres.2010.09.015.

Kollias, P., and B. Albrecht, 2005: Why the melting layer radar reflectivity is not bright at 94 GHz. *Geophys. Res. Lett.*, **32**, L24818, https://doi.org/10.1029/2005GL024074.

——, E. E. Clothiaux, M. A. Miller, B. A. Albrecht, G. L. Stephens, and T. P. Ackerman, 2007: Millimeter-wavelength radars: New frontier in atmospheric cloud and precipitation research. *Bull. Amer. Meteor. Soc.*, **88**, 1608–1624, https://doi.org/10.1175/BAMS-88-10-1608.

——, E. Luke, M. Oue, and K. Lamer, 2020: Agile adaptive radar sampling of fast-evolving atmospheric phenomena guided by satellite imagery and surface cameras. *Geophys. Res. Lett.*, **47**, e2020GL088440, https://doi.org/10.1029/2020GL088440.

Kumjian, M. R., and A. D. Schenkman, 2014: The curious case of ice pellets over middle Tennessee on 1 March 2014. *J. Oper. Meteor.*, **2**, 209–213, https://doi.org/10.15191/nwajom.2014.0217.

——, and K. A. Lombardo, 2017: Insights into the evolving microphysical and kinematic structure of northeastern U.S. winter storms from dual-polarization Doppler radar. *Mon. Wea. Rev.*, **145**, 1033–1061, https://doi.org/10.1175/MWR-D-15-0451.1.

——, S. M. Ganson, and A. V. Ryzhkov, 2012: Freezing of raindrops in deep convective updrafts: A microphysical and polarimetric model. *J. Atmos. Sci.*, **69**, 3471–3490, https://doi.org/10.1175/JAS-D-12-067.1.

——, A. V. Ryzhkov, H. D. Reeves, and T. J. Schuur, 2013: A dual-polarization radar signature of hydrometeor refreezing in winter storms. *J. Appl. Meteor. Climatol.*, **52**, 2549–2566, https://doi.org/10.1175/JAMC-D-12-0311.1.

——, D. M. Tobin, M. Oue, and P. Kollias, 2020: Microphysical insights into ice pellet formation revealed by fully-polarimetric Ka-band Doppler radar. *J. Appl. Meteor. Climatol.*, **59**, 1557–1580, https://doi.org/10.1175/JAMC-D-20-0054.1.

Leinonen, J., and A. von Lerber, 2018: Snowflake melting simulation using smoothed particle hydrodynamics. *J. Geophys. Res. Atmos.*, **123**, 1811–1825, https://doi.org/10.1002/2017JD027909.

Li, H., and D. Moisseev, 2020: Two layers of melting ice particles within a single radar bright band: Interpretation and implications. *Geophys. Res. Lett.*, **47**, e2020GL087499, https://doi.org/10.1029/2020GL087499.

Mason, B. J., 1956: On the melting of hailstones. *Quart. J. Roy. Meteor. Soc.*, **82**, 209–216, https://doi.org/10.1002/qj.49708235207.

Matrosov, S. Y., A. J. Hemysfield, and Z. Wang, 2005: Dual-frequency radar ratio of nonspherical atmospheric hydrometeors. *Geophys. Res. Lett.*, **32**, L13816, https://doi.org/10.1029/2005GL023210.

Mishchenko, M. I., 2000: Calculation of the amplitude matrix for a nonspherical particle in a fixed orientation. *Appl. Opt.*, **39**, 1026–1031, https://doi.org/10.1364/AO.39.001026.

Moisseev, D. N., S. Lautaportti, J. Tyynela, and S. Lim, 2015: Dual-polarization radar signatures in snowstorms: Role of snowflake aggregation. *J. Geophys. Res. Atmos.*, **120**, 12644–12655, https://doi.org/10.1002/2015JD023884.

Nagumo, N., A. Adachi, and H. Yamauchi, 2019: Geometrical properties of hydrometeors during the refreezing process and their effects on dual-polarized radar signals. *Mon. Wea. Rev.*, **147**, 1753–1768, https://doi.org/10.1175/MWR-D-18-0278.1.

NOAA, 1998: Automated Surface Observing System (ASOS) user's guide. National Weather Service Doc., 74 pp., https://www.weather.gov/media/asos/aum-toc.pdf.

Oue, M., P. Kollias, E. P. Luke, and J. Mead, 2017: A new Ka-band scanning radar facility: Polarimetric and Doppler spectra measurements of snow events. *2017 Fall Meeting*, New Orleans, LA, Amer. Geophys. Union, Abstract A31G-2270, https://agu.confex.com/agu/fm17/meetingapp.cgi/Paper/276182.

——, ——, S. Y. Matrosov, A. Battaglia, and A. V. Ryzhkov, 2021: Analysis of the microphysical properties of snowfall using scanning polarimetric and vertically pointing multi-frequency Doppler radars. *Atmos. Meas. Tech.*, **14**, 4893–4913, https://doi.org/10.5194/amt-14-4893-2021.

Phillips, V. T. J., A. Khain, N. Benmoshe, and E. Ilotoviz, 2014: Theory of time-dependent freezing. Part I: Description of scheme for wet growth of hail. *J. Atmos. Sci.*, **71**, 4527–4557, https://doi.org/10.1175/JAS-D-13-0375.1.

——, ——, ——, ——, and A. Ryzhkov, 2015: Theory of time-dependent freezing. Part II: Scheme for freezing raindrops and simulations by a cloud model with spectral bin microphysics. *J. Atmos. Sci.*, **72**, 262–286, https://doi.org/10.1175/JAS-D-13-0376.1.

Plummer, D. M., S. Göke, R. M. Rauber, and L. Di Girolamo, 2010: Discrimination of mixed- versus ice-phase clouds using dual-polarization radar with application to detection of aircraft icing regions. *J. Appl. Meteor. Climatol.*, **49**, 920–936, https://doi.org/10.1175/2009JAMC2267.1.

Pruppacher, H. R., and J. D. Klett, 1997: *Microphysics of Clouds and Precipitation*. 2nd ed. Oxford University Press, 954 pp.

Rahman, K., and F. Y. Testik, 2020: Shapes and fall speeds of freezing and frozen raindrops. *J. Hydrometeor.*, **21**, 1311–1331, https://doi.org/10.1175/JHM-D-19-0204.1.

Rauber, R. M., M. K. Ramamurthy, and A. Tokay, 1994: Synoptic and mesoscale structure of a severe freezing rain event: The St. Valentine's Day ice storm. *Wea. Forecasting*, **9**, 183–208, https://doi.org/10.1175/1520-0434(1994)009<0183:SAMSOA>2.0.CO;2.

——, L. S. Olthoff, M. K. Ramamurthy, D. Miller, and K. E. Kunkel, 2001: A synoptic weather pattern and sounding-based climatology of freezing precipitation in the United States east of the Rocky Mountains. *J. Appl. Meteor. Climatol.*, **40**, 1724–1747, https://doi.org/10.1175/1520-0450(2001)040<1724:ASWPAS>2.0.CO;2.

Ray, P. S., 1972: Broadband complex refractive indices of ice and water. *Appl. Opt.*, **11**, 1836–1844, https://doi.org/10.1364/AO.11.001836.

Reeves, H. D., and J. Waters, 2019: Dual-polarized radar coverage in terminal airspaces and its effect on interpretation of winter weather signatures: Current capabilities and future recommendations. *J. Appl. Meteor. Climatol.*, **58**, 165–183, https://doi.org/10.1175/JAMC-D-18-0123.1.

——, A. V. Ryzhkov, and J. Krause, 2016: Discrimination between winter precipitation types based on spectral-bin microphysical modeling. *J. Appl. Meteor. Climatol.*, **55**, 1747–1761, https://doi.org/10.1175/JAMC-D-16-0044.1.

Ryzhkov, A. V., and D. S. Zrnić, 2019: *Radar Polarimetry for Weather Observations*. 1st ed. Springer, 486 pp.

——, M. Pinsky, A. Pokrovsky, and A. Khain, 2011: Polarimetric radar observation operator for a cloud model with spectral microphysics. *J. Appl. Meteor. Climatol.*, **50**, 873–894, https://doi.org/10.1175/2010JAMC2363.1.

——, P. Zhang, H. Reeves, M. Kumjian, T. Tschallener, S. Trömel, and C. Simmer, 2016: Quasi-vertical profiles: A new way to look at polarimetric radar data. *J. Atmos. Oceanic Technol.*, **33**, 551–562, https://doi.org/10.1175/JTECH-D-15-0020.1.

Serke, D. J., S. Ellis, J. Hubbert, D. Albo, C. Johnston, C. Coy, D. Adriaanson, and M. Politovich, 2013: In-flight icing hazard detection with dual and single polarimetric moments from operational NEXRADs. *36th Conf. on Radar Meteorology*, Breckenridge, CO, Amer. Meteor. Soc., 15A.4, https://ams.confex.com/ams/36Radar/webprogram/Paper228592.html.

Smith, P. L., 1984: Equivalent radar reflectivity factors for snow and ice particles. *J. Climate Appl. Meteor.*, **23**, 1258–1260, https://doi.org/10.1175/1520-0450(1984)023<1258:ERRFFS>2.0.CO;2.

Stull, R., 2011: Wet-bulb temperature from relative humidity and air temperature. *J. Appl. Meteor. Climatol.*, **50**, 2267–2269, https://doi.org/10.1175/JAMC-D-11-0143.1.

Szyrmer, W., and I. Zawadzki, 1999: Modeling of the melting layer. Part I: Dynamics and microphysics. *J. Atmos. Sci.*, **56**, 3573–3592, https://doi.org/10.1175/1520-0469(1999)056<3573:MOTMLP>2.0.CO;2.

Tobin, D. M., and M. R. Kumjian, 2017: Polarimetric radar and surface-based precipitation-type observations of ice pellet to freezing rain transitions. *Wea. Forecasting*, **32**, 2065–2082, https://doi.org/10.1175/WAF-D-17-0054.1.

——, and ——, 2021: Microphysical and polarimetric radar modeling of hydrometeor refreezing. *J. Atmos. Sci.*, **78**, 1965–1981, https://doi.org/10.1175/JAS-D-20-0314.1.

——, ——, and A. W. Black, 2021: Effects of precipitation type on crash relative risk estimates in Kansas. *Accid. Anal. Prev.*, **151**, 105946, https://doi.org/10.1016/j.aap.2020.105946.

Van Den Broeke, M. S., D. M. Tobin, and M. R. Kumjian, 2016: Polarimetric radar observations of precipitation type and rate from the 2–3 March 2014 winter storm in Oklahoma and Arkansas. *Wea. Forecasting*, **31**, 1179–1196, https://doi.org/10.1175/WAF-D-16-0011.1.

Zerr, R. J., 1997: Freezing rain: An observational and theoretical study. *J. Appl. Meteor. Climatol.*, **36**, 1647–1661, https://doi.org/10.1175/1520-0450(1997)036<1647:FRAOAT>2.0.CO;2.